# Atomic Magnetometer Multisensor Array for rf Interference Mitigation and Unshielded Detection of Nuclear Quadrupole Resonance

Robert J. Cooper, David W. Prescott, Peter Matz, and Karen L. Sauer[*]
*Department of Physics and Astronomy, George Mason University, Fairfax, Virginia 22030, USA*

Nezih Dural and Michael V. Romalis
*Department of Physics, Princeton University, Princeton, New Jersey 08544, USA*

Elizabeth L. Foley and Thomas W. Kornack
*Twinleaf, 59 Snowden Lane, Princeton, New Jersey 08540, USA*

Mark Monti and Jeffrey Okamitsu
*NIITEK, 23031 Ladbrook Drive, Dulles, Virginia 20166, USA*

(Received 10 August 2016; revised manuscript received 26 August 2016; published 27 December 2016)

An array of four $^{87}$Rb vector magnetometers is used to detect nuclear quadrupole resonance signals in an unshielded environment at 1 MHz. With a baseline of 25 cm, the length of the array, radio-frequency interference mitigation is also demonstrated; a radio-station signal is suppressed by a factor of 20 without degradation to the signal of interest. With these compact sensors, in which the probe beam passes through twice, the fundamental limit to detection sensitivity is found to be photon-shot noise. More passes of the probe beam overcome this limitation. With a sensor of similar effective volume, 0.25 cm$^3$, but 25 × more passes, the sensitivity is improved by an order of magnitude to $1.7 \pm 0.2$ fT/$\sqrt{\text{Hz}}$.

DOI: 10.1103/PhysRevApplied.6.064014

## I. INTRODUCTION

Atomic magnetometers hold the promise of excellent sensitivity for the detection of rf magnetic fields oscillating in the high-frequency band [1] or lower [2]. Potential applications are widespread and include biomagnetics [3–10], geomagnetics [11], low-field NMR [12–14], magnetic resonance imaging [15,16], and nuclear quadrupole resonance (NQR). Towards the latter application, a potassium magnetometer with a sensitivity of 0.24 fT/$\sqrt{\text{Hz}}$ was used to detect the fertilizer explosive ammonium nitrite at 0.423 MHz in a shielded environment [17].

For frequencies higher than the high-frequency band, standard Faraday coil detection becomes more sensitive. At lower frequencies, superconducting quantum interference devices (SQUIDs) [18] and atomic magnetometers rival one another for better sensitivity [11,17,19]. Adoption of SQUIDs is hampered by the need for cryogenics for operation. Atomic magnetometers do not require cryogenic refrigeration and are, furthermore, insensitive to electric field noise. They do, however, tend to be rather large to take advantage of a high number of alkali atoms in the sensor [20]; for the ammonium nitrite measurement [17] the cell was 100 cm$^3$. More recently, a 1 cm$^3$ rf Rb magnetometer was demonstrated to have a 5 fT/$\sqrt{\text{Hz}}$ sensitivity [21], showing how scaling down the volume can have a detrimental effect. One way to have a small volume, but retain sensitivity, is to have the probe light pass through the cell multiple times [22,23]. We demonstrate two such magnetometers, one in which the beam passes through twice a 0.36-cm$^3$ volume of Rb vapor, made by Twinleaf, and another in which the beam passes through 50 times a 0.25-cm$^3$ volume, made by the Romalis group at Princeton. The former has a sensitivity of 14 fT/$\sqrt{\text{Hz}}$ and the latter 1.7 fT/$\sqrt{\text{Hz}}$. Quantum fluctuations such as photon-shot, light-shift, and spin-projection noise fundamentally limit the sensitivities of the magnetometers. An in-depth analysis of the fundamental and nonfundamental noise contributions, and the limitations they present, is discussed.

The sensitivity of the atomic magnetometers can easily be taken advantage of in shielded enclosures, but many applications, like NQR used for the detection of illicit substances, would be more fieldable if done unshielded. It has been shown that the superior sensitivity of the rf magnetometer can be retained unshielded if operated with two effective sensors and used as a gradiometer [24]. In that work, however, the two sensors were two channels within a larger cell and represented a baseline of only 2 cm; more recently, a similar gradiometer measurement was made with separate sensors 5.6 cm apart, but at a much lower frequency and worse sensitivity [25]. When distinguishing a local source of magnetic field, as from an NQR sample, from far-away sources, as from a radio station, a larger

---

[*] Corresponding author.
ksauer1@gmu.edu

baseline allows for the better measurement of a big sample; the signal falls off roughly as $(s/r)^3$, where $s$ is the size of the sample, and $r$ is the distance from the sample center. We demonstrate an array of four separate 2-pass sensors with a baseline of 25 cm, the distance between the outer two sensors, and arranged so as to be able to get rid of interfering signals while retaining the locally generated signal of interest. Using the signal from a local radio station, we demonstrate the ability to reduce interference by a factor of 20, limited by reradiation of the radio interference from our field coils.

Interference suppression using atomic magnetometers is fundamentally different from that with coils. An array of $N$ coils does not represent $N$ independent sensors because of a mutual inductance between the coils, although through decoupling methods [26] the mutual inductance can be minimized, but not completely eliminated. Often the focus for detection in the midst of interference is, therefore, on a single coil with multiple loops designed to have no net magnetic dipole moment, so that constant interference is rejected while some signal from the sample is detected, for instance in a "butterfly" [27,28] or two-coil coaxial [29] construction. A significant difficulty with this type of gradiometer arises from the capacitive coupling of one loop of the coil to the environment so that the zero-dipole moment is compromised [29]. Atomic magnetometers have no inductive coupling between sensors and no capacitive coupling to the environment. In addition, signals are obtained from each magnetometer so that real-time calibration is easily implemented and the balance between sensors continually maintained. Moreover, with multiple magnetometers, as we show here, not only can the common mode interference be rejected but also linearly varying interference.

We, furthermore, demonstrate the unshielded detection of sodium nitrite ($NaNO_2$), $s \sim 2.5$ cm, by NQR. This represents the first detection of NQR with atomic sensors in unshielded conditions. Besides being unshielded, a major difference between this and the original detection of NQR with atomic magnetometers [17] is the use of pulsed pump beams. Previously the destructive effects of the strong excitation pulse, ~1 mT, on the alkali polarization was mitigated by detuning the magnetometer during rf excitation and creating a one-sided excitation coil. With this current work, the destruction of the polarization during the rf excitation pulse is accepted. Polarization is regained using a strong pump light pulsed on after the rf pulse, but before detection of the NQR signal, thus simplifying the setup, particularly for multiple sensors.

While we demonstrate the detection of naturally abundant $^{14}$N, nuclear spin $I = 1$, NQR is a type of zero-field rf spectroscopy, often known as zero-field NMR, that can be used to detect any quadrupolar nuclei, $I > 1/2$, within a solid sample [30]. While the requirement $I > 1/2$ is a limitation, the quadrupolar nuclei are 3× as numerous as spin-$1/2$ nuclei [31]. Furthermore, the NQR frequencies are determined by the local electric-field gradient at the nucleus due to the surrounding structure and therefore provide a virtually unique spectral signature for the material [32]. NQR can also be done on powdered samples without broadening of the linewidth. This, coupled with the unique spectral signature, and the relatively simple equipment for excitation, makes NQR attractive for a variety of applications, such as the detection of $^{14}$N, $^{35}$Cl, $^{79}$Br, $^{81}$Br, and $^{39}$K in explosives [33–35] and narcotics [36]; pharmaceutical applications including crystallinity control, polymorph identification, and quantification of active ingredients [37–39]; and the study of motion and phase transitions in superconductors and ferroelectric materials [40–43]. Any of these applications would become more versatile if allowed to sensitively operate in an unshielded environment as presented here.

## II. EXPERIMENTAL DESIGN

### A. Sensors

The atomic magnetometers operate in a crossed pump-probe configuration and contain isotopically enriched $^{87}$Rb. The desired saturated vapor density is created by heating the oven to $T > 130\,^{\circ}\mathrm{C}$, Table I, either through heated air flow, as with the 50-pass sensor, or, much more unconventionally, through optical means, as is the case with the 2-pass sensors. The temperature sensor of the 2-pass sensor is also fiber optic, making for an entirely fiber-coupled magnetometer as shown in the inset of Fig. 1. Neon gas, at a number density of 0.8 amg, is used as a buffer gas to slow diffusion to the walls, and between 0.05–0.06 amg of $N_2$ is added as a quenching gas [44]. The active volumes are quite small, $10 \times 5 \times 5$ mm$^3$ for the 50-pass sensor and $10 \times 6 \times 6$ mm$^3$ for the 2-pass sensor, with the longest dimension corresponding to the probe direction. The mirrors for the 50-pass magnetometer are curved [23] and are internal to the vapor cell, while those of the 2-pass magnetometer are flat and are external to the vapor cell. The 2-pass cells have been quite robust over time, while the internal mirrors in the 50-pass magnetometer show some degradation on several weeks time scale. The robustness of the mirror coatings is improved by using an $Al_2O_3$ outer-layer coating [22]. Higher-quality dielectric films using ion-beam sputtering film deposition also improve the robustness of the mirrors.

The alkali atoms become highly polarized under illumination by circularly polarized light at the $D_1$ resonance. For the 50-pass sensor the circularly polarized pump beam travels through free space and is shaped into a top-hat profile large enough to fill the cell. The 2-pass sensor is fiber coupled through a multimode fiber to create a spatially uniform beam; at the fiber exit a ball lens, a pair of beam splitters, and a pair of $\lambda/4$ wave plates are used to shape and circularly polarize the beam. Resulting polarizations can be found in Table I. The pump laser is turned off during data acquisition to obtain better sensitivity. Control of the pump is done through the tapered amplifier for the 2-pass sensors,

TABLE I. Sensor characteristics are given for the 2-pass cells, Fig. 1, and the 50-pass cell. The effective cell temperature $T$ is determined experimentally; $T$ matches the oven set point for the 50-pass cell, but is smaller than the 2-pass set point, 200 °C, due to one-sided heating of the vapor cell. Light of power $\Phi_{\mathrm{pm}}$ pumped the cell to polarization $P$, while a low power beam, of power $\Phi^0_{\mathrm{pr}}$, probed the transverse spin state; high $P$ leads to a longer decay time $T_{2H}$, Fig. 9. The 50-pass cell is shielded and measured at resonant frequency of 1.00 MHz; the 2-pass cell is unshielded and measured at 1.3 MHz, 10 kHz away from the radio interference. Furthermore, sensitivity for two orthogonal orientations of the horizontal linear array, ⊥ and ∥, are measured and used an acquisition window of 1 ms with time-domain filtering.

| Sensor number | $T$ (°C) | $T_{2H}$ @ 5 ms (ms) | $P$ @ 5 ms (%) | $\Phi_{\mathrm{pm}}$ (W) | $\Phi^0_{\mathrm{pr}}$ (mW) | $\Phi_{\mathrm{pr}}$ at diodes (mW) | $S_\perp$ (fT/$\sqrt{\mathrm{Hz}}$) | $S_\parallel$ (fT/$\sqrt{\mathrm{Hz}}$) |
|---|---|---|---|---|---|---|---|---|
| | | | | *2-pass sensors* | | | | |
| Inner 1 | 139 | 0.23 | $67 \pm 5$ | 0.21 | 1.6 | 0.4 | $21 \pm 2$ | $26 \pm 3$ |
| Inner 2 | 136 | 0.28 | $65 \pm 6$ | 0.21 | 1.1 | 0.3 | $14 \pm 2$ | $21 \pm 2$ |
| Outer 1 | 134 | 0.33 | $61 \pm 5$ | 0.25 | 2.0 | 0.6 | $16 \pm 2$ | $27 \pm 3$ |
| Outer 2 | 131 | 0.50 | $85 \pm 5$ | 0.21 | 1.2 | 0.2 | $15 \pm 2$ | $29 \pm 3$ |
| | | | | *50-pass sensor* | | | | |
| | 156 | 0.53 | $92 \pm 1$ | 1.2 | 0.4 | 0.05 | $1.7 \pm 0.2$ | |

but through an acoustic optical modulator for the 50-pass sensors.

The probe beam is fiber coupled into the sensor through a polarization-maintaining fiber. A linear polarizer placed at the cell entrance enforces the polarization direction. For the 2-pass sensor, the exiting probe beam is also fiber coupled, while for the 50-pass sensor it is free space. A balanced polarimeter, consisting of a polarizing beam splitter and photodiode amplifiers, measures the final rotation of the probe light. The resulting signal is detected by a phase-sensitive spectrometer [45]. With the higher-number density and higher number of passes associated with the 50-pass cell, the signal is optimized with the probe wavelength farther off resonance, $\lambda_{\mathrm{pr}} = 795.64$ nm, than for the 2-pass cell $\lambda_{\mathrm{pr}} = 795.15$ nm.

### B. Fields

For the unshielded system, three pairs of nested square Helmholtz coils [46], with a side length of about 0.6 m and wrapped around a plastic frame, are used to compensate for the Earth's magnetic field and set the Larmor frequency $f_0 = B_0\gamma/(2\pi)$, where $\gamma$ is the atomic gyromagnetic ratio $\gamma/(2\pi) = 7$ MHz/mT. The array of 2-pass sensors, Fig. 1, is centered inside these field coils. Six coils, wrapped around an individual sensor, provide a fine control of the local static fields $[B_x, B_y, B_z]$ as well as the gradient of $B_z$; the coils encased in polyimide film can be seen in the inset of Fig. 1. Orthogonal fields $[B_x, B_y]$ are chosen to minimize the Larmor frequency, while $B_z$ is chosen to set the Larmor frequency to the frequency of interest. The field gradient is chosen to optimize the signal in each sensor. These "per-sensor" field coils are controlled by the shim unit associated with the spectrometer. The wire pair for each field coil is threaded through multiple ferrite toroidal cores in such a way as to choke out both common mode and differential ac signals, including those due to the radio interference. In addition, shielding is placed over the chokes and wiring. Furthermore, controls and current supplies for all

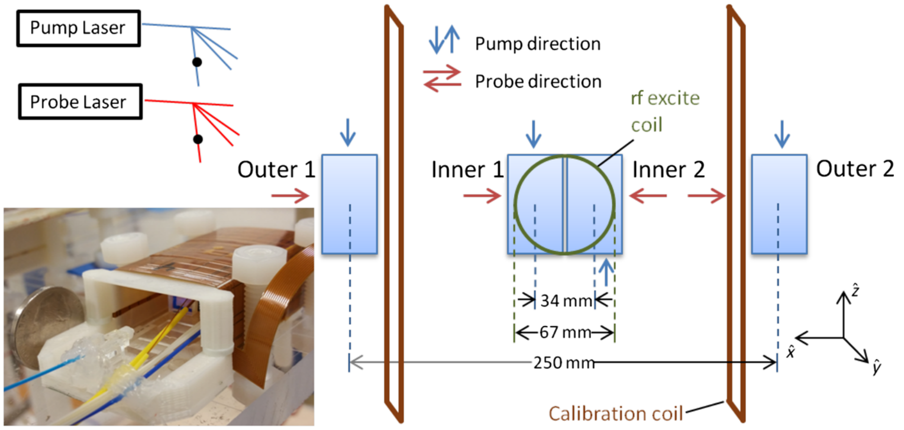

FIG. 1. Top view of the 2-pass sensor array. In the inset, a Twinleaf sensor, held down with nylon bolts, is shown with a nickel for perspective; all connections, including those for heating and temperature measurement, are fiber optic. Table I gives the pump and probe powers measured at the fiber mating connectors, denoted by a black dot above. A square pair of coils, separation and side length of 21 cm, provide real-time calibration of the sensors, while the net static field $B_0\hat{z}$, which is kept parallel to the pump beam, is set by field coils that are not shown here. The NQR sample, sodium nitrite, sits inside the rf excitation coil and is situated 2 cm above the sensor array.

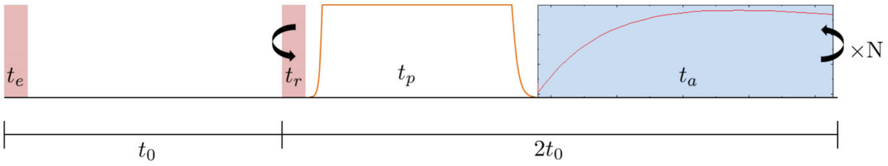

FIG. 2. A 90-90 spin-lock spin-echo sequence [52], rf duration $t_e = t_r = 100\ \mu$s, with $N$ echoes, is used to excite the sample. The $Q$ of the tuned excitation coil is spoiled, so that the stored energy quickly dissipates before the light of duration $t_p$ pumps the sensor. The light is adiabatically ramped down to avoid perturbations, before the signal is acquired during $t_a$. Values are given in Table II.

field coils are placed on an ac-line conditioner [47], eliminating random noise spikes in the spectrum. Data collection sequences are synchronized with the mains electricity for clear identification of effects associated with line power.

The 50-pass sensor is shielded in order to accurately explore the limits of its sensitivity. However, a set of coils is still used to control the local field—three $B_z$ gradient coils [48,49], two saddle coils for $[B_x, B_y]$ [50], and one for $B_z$ [51], all wrapped on an 8-inch-diameter and 16-inch-long G10 cylinder.

The spectrometer is also used to create rf pulses as well as to control the timing and shaping of the pump pulses, Fig. 2. For NQR excitation a 2-kW power amplifier is used to create the strong field in the excitation coil, Fig. 1. The same coil doubles as the source of the test signal in the Radio frequency interference mitigation (RFIM) measurements, but instead of amplification, attenuation is used to get signals on the order of 100 fT at the inner sensors. Real-time calibration of the sensors is critical for the detection of such small signals in an unshielded environment. Calibration is accomplished by comparison to signals from the calibration coil, Fig. 1, taken just before and after the measurement of interest. This coil is designed to give nearly equal signal over the four sensors and is itself calibrated using an electron spin resonance (ESR) experiment, Fig. 3. Details of the ESR experimental sequence can be found in Fig. 4 and Table III.

## III. RESULTS

### A. Sensor characterization

The 2-pass sensors are studied in an unshielded environment in two orthogonal orientations of the horizontal linear array with respect to the laboratory. In one, labeled the ⊥ orientation, the static $B_z$ field, which is aligned with the pump beam, Fig. 1, is stable. In the second, rotated by 90° from the first and labeled the ∥ orientation, the $B_z$ field, again aligned with the pump beam, had a significant 60-Hz contribution which resulted in the Larmor frequency periodically shifting, Fig. 5. Coincidentally, the interference from the radio station is greater in the ∥ orientation, Fig. 6(a). A 50-pass sensor, of similar active volume as the 2-pass sensor, is studied under a shielded environment, for direct comparison and motivation for future work on arrays with compact multipass sensors.

The sensors can be characterized by the contributing sources [53] to their limiting noise, some of which are fundamental in nature [20]—spin-projection, light-shift, and photon-shot noise—and some of which are not—environmental magnetic noise, ringing induced from termination of the pump beam, and technical noise from the photodiode amplifier. The baseline noise, that is the off-resonant noise seen in Fig. 6, is set by a combination of photon-shot and technical noise; the latter can be measured with the probe light off. On top of baseline noise, is added the resonant noise contributions. These can be difficult to detangle, although they carry their own characteristic signatures. For example, the presence of spin-projection

TABLE II. The sequence timing of Fig. 2 is given here, either with the NQR sample as the source of the signal or a small field from a coil, for instance, the square calibration or short solenoid coil of Fig. 1. Strong rf pulses, $B_1 = 1$ mT of duration $t_r$, are applied to the sample during the NQR detection, but not in other measurements; for simplification and higher overall polarization, see Fig. 8. For the unshielded 2-pass sensors, realtime calibration utilizes rf pulses of known strength, about 10 pT, applied before and after the echo train, Fig. 12. For the shielded 50-pass sensor, individual scans, not an echo train, are used for sensitivity measurements. (NA signifies not applicable.)

| Measurement type | $f_0$ (MHz) | Pump $t_p$ (ms) | Acquire $t_a$ (ms) | Spacing $t_0$ (ms) | Echoes $N$ | Signal source |
|---|---|---|---|---|---|---|
| | | | *2-pass sensors* | | | |
| NQR SLSE | 1.03 | 1.0 | 1.3 | 2.4 | 120 | 63 g of $NaNO_2$ |
| NQR calibration | 1.03 | 1.0 | 1.3 | 2.4 | 60 | calibration coil |
| RFIM “signal” | 1.3 | 0.8 | 1.0 | 2.0 | 1000 | small solenoid |
| RFIM calibration | 1.3 | 0.8 | 1.0 | 2.0 | 200 | calibration coil |
| | | | *50-pass sensor* | | | |
| Sensitivity data | 1.0 | 1.0 | 1.0 | NA | 100 | saddle coil |

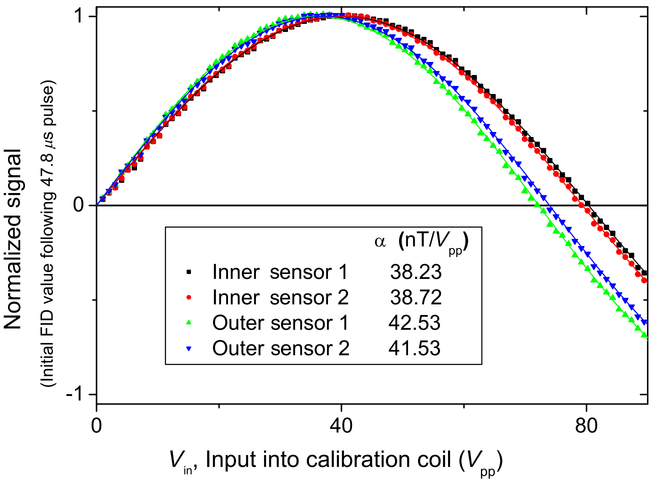

FIG. 3. The ESR calibration for the calibration coil, Fig. 1, determines the field values in the 2-pass sensors for the measured voltage input $V_{\rm in}$. Normalized data are fit to $\sin(\gamma\alpha V_{\rm in} t_{\rm rf}/2)$, where the calibration constant $\alpha$ is given in the legend. Data are taken with the oven at a reduced set point, 100 °C, to avoid nonlinearity in the measurement.

TABLE III. Sensor characterization values of Fig. 4 are given for the 2-pass sensor (50-pass sensor in parenthesis). Short pulse lengths $t_{\rm rf}$ are used for all measurements, corresponding to small tip angles $\gamma B_1 t_{\rm rf} \ll 0.01$ for vary-$\tau$ and buildup measurements, but with the use of an rf amplifier, large tip angles for the ESR calibration.

| | Pump $t_p$ (ms) | rf pulse $t_{\rm rf}$ ($\mu$s) | $\tau$ (ms) |
|---|---|---|---|
| Buildup | Variable | 12 (12) | 0 |
| Vary-$\tau$ | 5 (5) | 30 (10) | Variable |
| ESR | 5 (5) | 48 (12) | 0 |

noise is discernible as a slightly off-resonance "bump" when the cell is not pumped [54]; such a bump is only observed for the 50-pass cell with a high probe power, Fig. 6(b). The noise bump due to quantum fluctuations of unpolarized atoms is shifted from the resonance for nearly fully polarized atoms due to the nonlinear Zeeman effect. It is shifted by 560 ± 170 Hz from resonance, in agreement with the 438 Hz predicted for $f_0 = 1$ MHz. For another example, light-shift noise decreases with the probe intensity [20]; the noise for the 50-pass sensor is minimized at a low probe power, Fig. 6(c) and Table I. Further, abrupt termination of the pump pulse yields high noise levels which can be greatly reduced by adiabatically turning off the light so that any created magnetization realigns with the static field. An additional method to reduce the effects of ringing is to use matched filtering, that is, multiplication of the signal by its own shape; the filter function $(1 - e^{-t/\tau_f})$ with $\tau_f = 0.25$ ms is used. In cases where ringing makes a significant contribution to the overall noise, even after adiabatic ramp-down of the pump pulse, filtering is effective, for example, Fig. 6(c). Environmental magnetic noise, including radio interference, can be reduced by the application of interference algorithms with multiple sensors or can be shielded out for a single sensor.

For the unshielded 2-pass sensors at a frequency of 1.3 MHz, the *relative* ratio of noise powers, averaged over the four sensors, is

$$\begin{array}{lcccccccl} [\text{unfiltered} & : & \text{filtered} & : & \text{baseline} & : & \text{technical}] & & = \\ [1.7 & : & 1.3 & : & \mathbf{1} & : & 0.3] & & (\perp \text{ orientation}) \\ [2.2 & : & 2.1 & : & \mathbf{1} & : & 0.3] & & (\parallel \text{ orientation}). \end{array}$$

Figure 6(a) shows the *absolute* noise values for inner sensor 2, which has the smallest baseline noise of the 2-pass sensors, 11 $\mathrm{fT}/\sqrt{\mathrm{Hz}}$, when placed in the $\perp$ orientation. The case of being quite close in frequency to the radio station is treated separately in the following section. Judging by the asymmetric baseline for the $\parallel$ orientation in Fig. 6(a), it is clear that the interference is measurable even at 1.3 MHz, outside of the ±5-kHz radio bandwidth nominally allotted to the station WDCT, 1310 AM; in the $\perp$ orientation the baseline is not asymmetric and there is no observable peak at 1.31 MHz. Therefore, environmental noise is significant for the $\parallel$ direction, while ringing seems to be more of an issue for the $\perp$ direction. In either orientation, upon application of interference rejection, as explained in detail in Sec. III B, the noise is reduced down to the baseline limit: $14 \pm 1$ $\mathrm{fT}/\sqrt{\mathrm{Hz}}$ for $\perp$ and $19 \pm 2$ $\mathrm{fT}/\sqrt{\mathrm{Hz}}$ for $\parallel$; the baseline limit is dominated by photon-shot noise, which can be calculated by subtracting out the technical noise. The increase in baseline noise for the $\parallel$ direction is due to the 60-Hz field contribution to the total field. In principle, such field variation can be nulled out by using a dc magnetometer to measure the local field and correcting for it in real time.

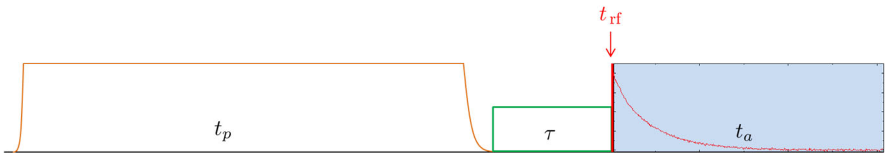

FIG. 4. By varying light duration $t_p$ the polarization buildup rate can be measured, Fig. 8. By varying $\tau$, the time in the dark after the polarization is fully built up, relaxation rates which characterize the sensor can be determined, Fig. 9 and Table I. By varying the rf pulse strength, Fig. 3, the magnetic field can be calibrated. Details for buildup, vary-$\tau$, and ESR experiments can be found in Table III.

For the shielded 50-pass sensor at a frequency of 1 MHz, the *relative* ratio of noise powers is

$$\begin{array}{lclclclclcl} [\text{unfiltered} & : & \text{filtered} & : & \text{unpumped} & : & \text{baseline} & : & \text{technical}] & & = \\ [12.9 & : & 10.8 & : & 2.3 & : & \mathbf{1} & : & 0.3] & & (1.2\ \text{mW},\ 795.69\ \text{nm}) \\ [4.0 & : & 2.9 & : & 1.5 & : & \mathbf{1} & : & 0.7] & & (0.4\ \text{mW},\ 795.64\ \text{nm}). \end{array}$$

Figures 6(b) and 6(c) show the *absolute* noise values for the 50-pass sensor under the two different probe powers. Here, the baseline corresponds to the case when the field is detuned, by 250 kHz, from the detection frequency, avoiding potential noise contributions from spin-projection noise. With the higher probe power the filtered sensitivity is 2.1 $\mathrm{fT}/\sqrt{\mathrm{Hz}}$ and the lower 1.7 $\mathrm{fT}/\sqrt{\mathrm{Hz}}$, an order of magnitude better than the 2-pass cells. Previous measurements [53] in the nested trio of mu-metal shields with a more sensitive, but much larger, K magnetometer suggest that ambient noise is most likely negligible. While all other sources of noise are non-negligible, it is clear from the ratio of noise powers, that photon-shot noise (the difference between the baseline and technical noise) gives a smaller contribution than spin-projection noise (approximately the difference between the unpumped and baseline noise) and light-shift noise. The upper limit for light-shift noise is the difference between the filtered and unpumped noise. Noise estimates, as well as the dependence of the sensitivity on probe power, indicate we are in a regime in which the light-shift noise is comparable to that of spin-projection noise.

To understand the basic difference between the two types of sensors, it is important to look at photon-shot noise, the fundamental limiting noise of the 2-pass sensor. With shot noise, the sensitivity is [20]

$$\delta B_{\mathrm{psn}} = \frac{\sqrt{2}}{\gamma T_2 \theta_{\max} \sqrt{\phi_{\mathrm{pr}} \eta}}, \tag{1}$$

where $\phi_{\mathrm{pr}}$ is the flux of probe beam photons arriving at the photodiodes, $\eta$ is the photodiode quantum efficiency, and $T_2$ is the characteristic time for the transverse electron

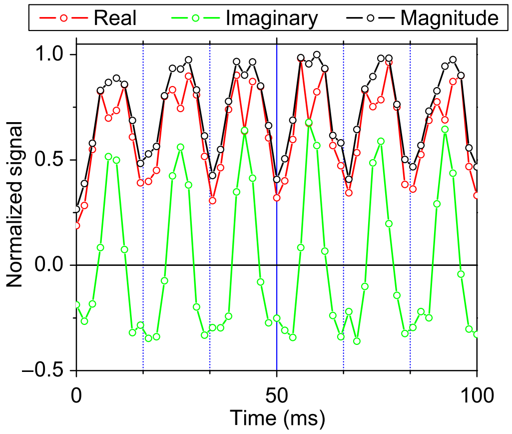

FIG. 5. In the ∥ orientation, a 60-Hz magnetic field is found to oscillate the resonance frequency of the magnetometer by ±2 kHz, resulting in a fluctuation in the phase and size of the complex signal, as shown above for inner sensor 1. The effect can also be seen in the large and periodic 60-Hz noise spikes in the inset of Fig. 10(b). Such examples of a 60-Hz noise can be found in other works [21].

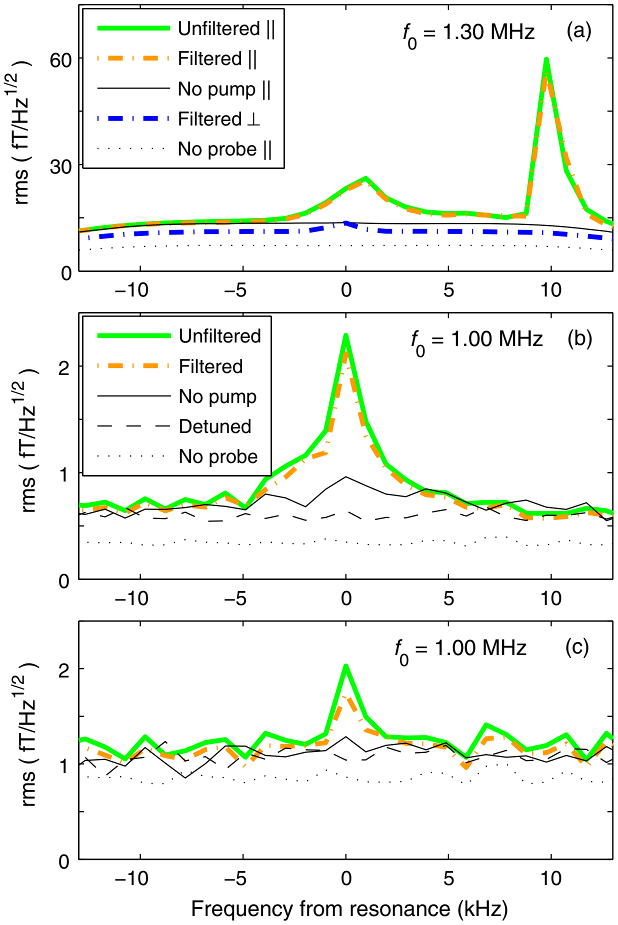

FIG. 6. The 50-pass sensor [(b), (c)] is an order of magnitude more sensitive than the 2-pass sensor. Representative data for the 2-pass sensors, taken using inner sensor 2, is shown in (a). (c) Low probe power, 0.4 mW, yields better sensitivity than (b) higher power, 1.2 mW. As discussed in the text, looking at noise with the pump or probe light turned off, with the field detuned, and under matched filtering gives insight into the dominant noise sources. Filtering is applied to all time domain data, duration 1 ms, except those explicitly labeled as unfiltered. Because of a long dwell time for (a), digital filtering effects can be observed towards the edges of the spectra.

polarization $P_T$, the observable in our system, to decay. The maximum optical rotation $\theta_{\max}$ is the rotation after a $\pi/2$ pulse,

$$\theta_{\max} = \frac{1}{2} r_e c f P n l D(\lambda_{\mathrm{pr}}), \tag{2}$$

where $r_e$ is the electron radius, $c$ is the speed of light, $f$ is the $D_1$ oscillator strength, $n$ is the number density, $P$ is the polarization, and $D(\lambda_{\mathrm{pr}})$ is the dispersion profile. The biggest difference between the 2-pass and 50-pass sensors is the effective length $l$ of the cell, which for the 2-pass sensor is 2 cm and for the 50-pass sensor, 50 cm. Taking into account $n$, $l$, $\lambda_{\mathrm{pr}}$, and $P$, $\theta_{\max}$ would be $1.1 \pm 0.2$ rad for fully pumped 2-pass sensors. Because the $\theta_{\max} \gg \pi$ for the 50-pass, an accurate value of $\theta_{\max}$ is relatively straightforward to measure. From the balanced polarimeter the signal after an optical rotation of $\theta$ is proportional to $\sin\{2\theta\cos(\omega t)\}$, where $\omega$ is the frequency of the signal. After heterodyne detection the observed signal is proportional to $2J_1(2\theta)$ [55]. As shown in Fig. 7, $\theta_{\max} = 20.56 \pm 0.02$ rad. The $\pi/2$ pulse used lasted three periods of the Zeeman resonance frequency [23]. The order-of-magnitude increase in optical rotation accounts for the order-of-magnitude difference in sensitivity between the 2-pass and 50-pass cells.

In order to have the optimal $\theta_{\max}$, $P$ should be maximized. The polarization numbers given in Table III are after a 5-ms-long light pulse. From the buildup curves, shown in Fig. 8, it is clear that all sensors are close to their optimum polarization after 5 ms. However, in an echo train, it is not possible to accommodate such a long light pulse. For the sensitivity measurements and NQR measurements the pulses are kept close to 1 ms in duration. This time includes a quick ramp-up and a slower ramp-down to reduce the light ringing; the 2-pass sensor has a Gaussian ramp-down over 0.1 ms and the more-sensitive 50-pass sensor a ramp-down over 0.3 ms. For all sensors, but one, the sensors are close to having $P$ maximized after only a millisecond. Inner sensor 1 has a longer buildup time and suffers some degradation in sensitivity, Table I.

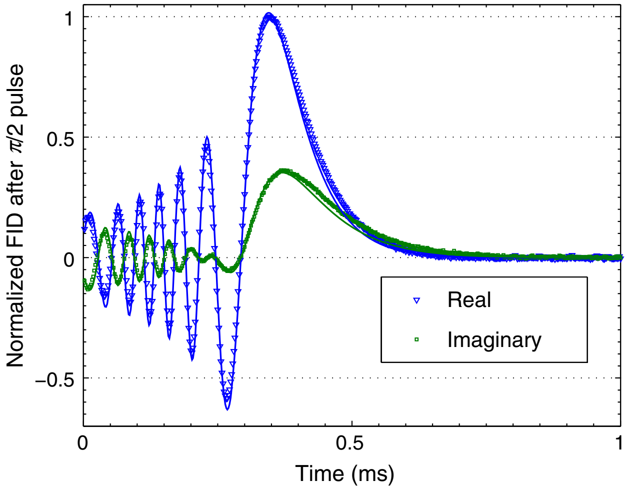

FIG. 7. The free induction decay (FID) of the signal under heterodyne detection after a $\pi/2$ pulse behaves as the Bessel function $J_1\{2\theta(t)\}e^{i\Delta\omega t+\varphi}$, solid lines, where $\Delta\omega$ is the angular off resonance from the spectrometer frequency, $\varphi$ is the receiver phase, and an analytic solution [56] for $\theta(t)$ is derived from Eq. (3) with $P = P_T$. From this fit it is found $\theta_{\max} = \theta(t=0) = 20.56 \pm 0.02$ rad.

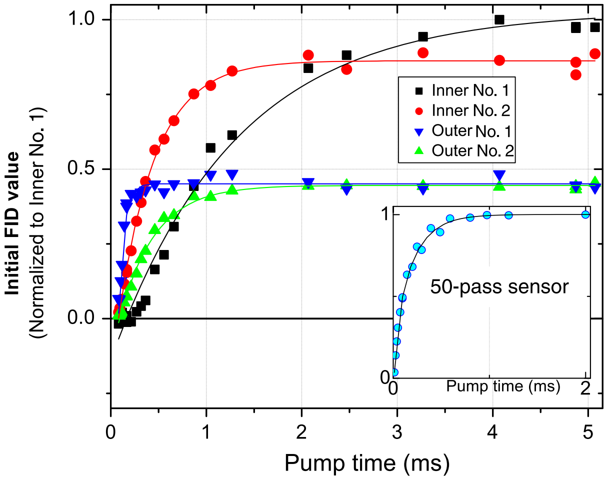

FIG. 8. The buildup of signal as a function of pump duration is shown for the 2-pass sensors in the main graph, and for the 50-pass sensor in the inset. The NQR data and sensitivity measurements are taken with pump times close to 1 ms, to accommodate the echo train timing.

As can be seen from Eq. (1), another way of increasing sensitivity is to have a high $T_2$. This time constant is highly dependent on the polarization $P$ of the alkali atoms. In fact, a metric of polarization is the line narrowing of the FID under high polarization. A clear example of this line narrowing is observable in Fig. 9, showing a factor of 8 line narrowing in the 50-pass sensor, corresponding to a polarization of $(92 \pm 1)\%$. The observed line narrowing for the 2-pass sensors is between 1.5–2.6, indicating a weaker polarization, between (61–85)%, Table I. Variations in the polarization $P$ are most likely due to a variation in the pump light distribution and power within each cell. In contrast to the fiber-coupled pump beam of the 2-pass sensor, the pumping of the 50-pass magnetometer is free space, allowing for an easier shaping of an intense beam to a top-hat shape. More formally, the evolution of the transverse electron polarization $P_T$, the observable in our system, can be described by [56]

$$\frac{dP_T}{dt} = -\frac{R_{\mathrm{SE}}(1-P)}{5} P_T - \frac{R_{\mathrm{SD}}}{4} P_T - \frac{1}{T_2^*} P_T, \tag{3}$$

when the net polarization $P$ is close to one. In the equation above, $R_{\mathrm{SD}}$ is the spin-destruction rate, $R_{\mathrm{SE}}$ the spin-exchange rate, and $1/T_2^*$ is the relaxation rate due to field

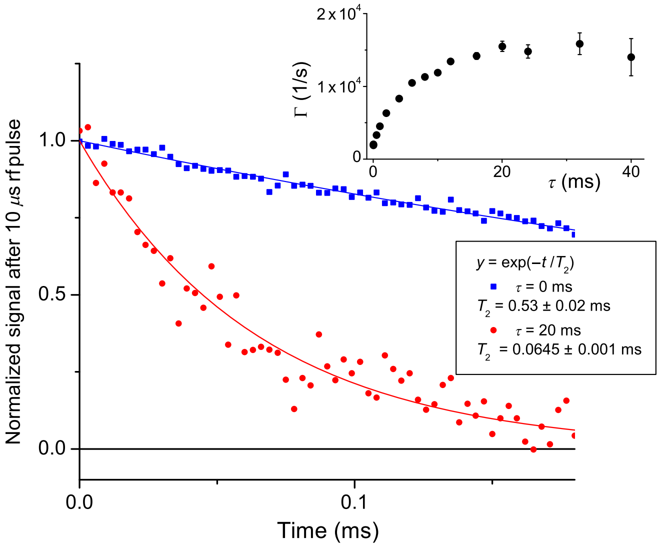

FIG. 9. The factor of 8 light narrowing reveals 92% spin polarization in the 50-pass cell, as measured at a 1-MHz Larmor frequency. The delay $\tau$ between the 5-ms-long light pulse and the resonant rf pulse, Fig. 4, is given in the legend, while the relaxation rate, $\Gamma = 1/T_2$, as a function of $\tau$ values is in the inset. The probe power used for this particular measurement is $3\times$ higher than what is listed in Table I.

inhomogeneity in the cell. Using a small tip angle on the highly polarized atoms, the transverse polarization is excited. Furthermore, observing on a time scale short with respect to $T_1$ relaxation, the evolution can then be described by a single time constant $T_{2H}$, $(dP_T/dt) = (-P_T/T_{2H})$, Table I. Therefore,

$$(1-P) = \frac{5}{R_{\mathrm{SE}}}\left(\frac{1}{T_{2H}} - \frac{1}{T_2^*} - \frac{R_{\mathrm{SD}}}{4}\right). \tag{4}$$

Under conditions of no pumping, or "in the dark", high temperature, low probe power, and low polarization the spin-destruction rate for $^{87}$Rb ($I = 3/2$) can be estimated to be $R_{\mathrm{SD}} = 6/T_1$, where $T_1$ is the spin-lattice relaxation time [57]. By pumping and then waiting for various time durations in the dark before excitation of the signal, $T_1$ can be measured. For the 2-pass sensors the time constant $T_1$ is about 10 ms and for the 50-pass sensor $T_1$ is 15 ms.

Under the same experimental conditions, the decay of the transverse polarization, characterized by $T_{2L}$, is dominated by alkali metal spin-exchange collisions [20], $R_{\mathrm{SE}} = 8[(1/T_{2L}) - (1/T_2^*) - (1/T_1)]$. For these measurements, the magnetic field is dropped to 21 $\mu$T to avoid the effects from the partially resolved Zeeman resonance observable at higher fields and low polarization. The rate $R_{\mathrm{SE}}$ can also be used to measure the Rb number density $n_{\mathrm{Rb}}$ and from there the effective temperature of the oven [58]. In particular, $R_{\mathrm{SE}} = n_{\mathrm{Rb}}\sigma_{\mathrm{SE}}v_{\mathrm{Rb}}$, where $v_{\mathrm{Rb}}$ is the relative velocity for the Rb atoms and the spin-exchange cross section [23] is $\sigma_{\mathrm{SE}} = 1.9\times10^{-14}$ cm$^2$. The Rb number densities range $3.8$–$5.7\times10^{13}$ cm$^{-3}$ within the 2-pass magnetometers, and are $1.4\times10^{14}$ cm$^{-3}$ for the 50-pass magnetometers. Number densities are limited by oven constraints and $\lambda_{\mathrm{pr}}$ is chosen to maximize the signal.

The time constant $T_2^*$ can be measured by reducing the temperature of the cell until the relaxation is dominated by field gradients. For instance, for the 2-pass sensors, we reduce the oven temperature, in celsius, by a factor of 2. For the field corresponding to $f_0 = 1.3$ MHz, the Zeeman resonance is resolved, and the linewidth reveals $T_2^* \sim 1$–$4$ ms, depending on the sensor.

With higher polarization and much higher optical rotation, the 50-pass sensor shows a sensitivity an order of magnitude better than the 2-pass sensors showing the potential of these very compact cells, active volume $<0.4$ cm$^3$. Fundamentally, the 2-pass sensor is dominated by photon-shot noise; the 50-pass sensor is not. For instance, for the inner sensor 2, Fig. 6(a), the experimentally determined photon-shot noise, 8.5 fT/$\sqrt{\mathrm{Hz}}$, is in good agreement with the predicted value, 8 fT/$\sqrt{\mathrm{Hz}}$, when the buildup time is taken into account; all other sources of fundamental noise are estimated to be less than 1 fT/$\sqrt{\mathrm{Hz}}$. The rest of this paper focuses on the capabilities of an array of sensors, in this case the 2-pass sensor, to reject interference and to measure NQR signals in an unshielded environment.

### B. Radio-frequency interference mitigation

Far off resonance from an interfering signal, the individual sensitivities are around 20 fT/$\sqrt{\mathrm{Hz}}$, Table I. As explained in more detail below, Figs. 10(a) and 10(b) show the 1D and 2D sensitivity, or standard deviation, of one of the interior sensors, inner sensor 1, at a resonance frequency $f_0 = 1.30$ MHz with the array in the $\parallel$ orientation. A signal of 100 fT observed for a total of 1 sec, that is, a thousand 1-ms concatenated acquisition windows, Fig. 2, is therefore easily observable in Figs. 10(a) and 10(b). In the presence of interfering signals the noise can increase greatly. The noise increases 40-fold at a resonance frequency of 1.31 MHz, the nominal transmitting frequency of the local radio station.

There are two ways that the data are represented in Fig. 10. To obtain 1D spectra, leftmost graphs, each of the thousand individual windows is averaged and then Fourier transformed to give a resolution of 1 kHz. To obtain 2D spectra, rightmost graphs, each individual window is Fourier transformed and the resonant peak is picked out. The resulting array of a thousand peaks has data points spaced 2 ms apart. This array is then discretely Fourier transformed to give the 2D spectra. The resulting spectrum is 0.5 Hz, 3 orders of magnitude smaller than for the 1D spectra. The on-resonance values of the 1D and 2D spectrums can be shown to be mathematically equivalent,

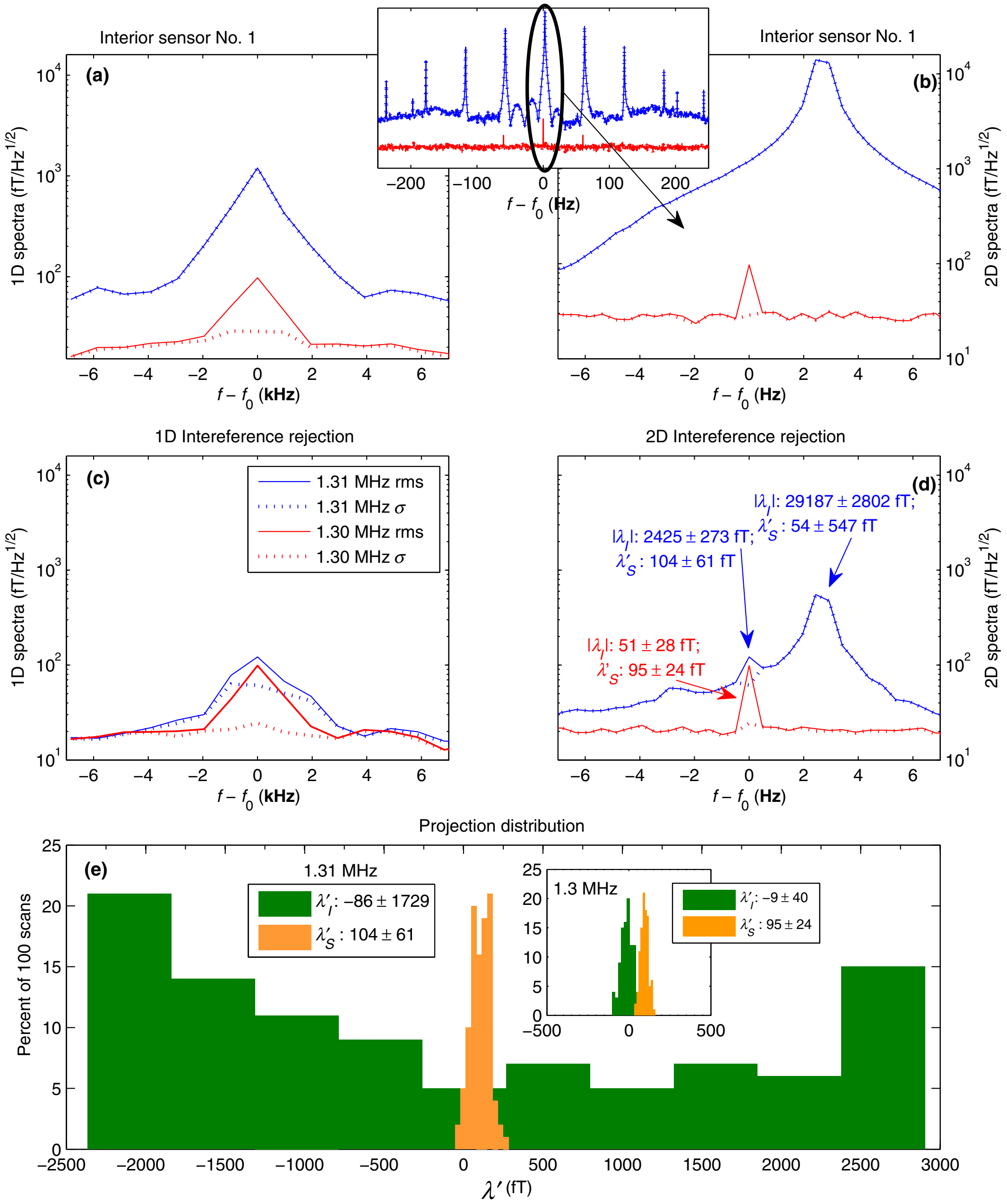

FIG. 10. When the resonance frequency is matched to a radio station, blue lines, the 100-fT test signal is lost in the interference, as can be seen in both the 1D spectra (a) and the 2D spectra (b). The standard deviation about the mean $\sigma$ of the 100 scans, dashed lines, is indistinguishable from the root mean square of the data, rms. Using all four sensors, and the rejection algorithm described in the text, the signal can now be distinguished from the interference (c) and (d), and can be compared to the case when there is little interference, red lines. (e) Looking at the on-resonance projection coefficients, $\lambda_S = \lambda'_S + i\lambda''_S$ for the signal and $\lambda_I = \lambda'_I + i\lambda''_I$ for interference, one can clearly see the signal separated out from the interference distribution.

which can be observed in Fig. 10. The 2D spectrum, however, is able to give more information as to the source of the interference. In Fig. 10(b), blue lines, one can see that a major source of interference is 14 $\mathrm{pT_{rms}}$ at a frequency of 2.5 Hz above 1.31 MHz, in contrast to a 200× smaller resonant test signal. The large interference peak corresponds to the radio station's carrier signal. The inset of Fig. 10(b) shows a wider view of Fig. 10(b); the center peak is again the carrier signal, the other periodically repeating peaks are the 60-Hz artifacts previously mentioned, while the original information being transmitted through the radio is contained in the low-level side bands, which nominally extend out to ±5 kHz and are symmetric around the carrier frequency.

This increase in noise due to interference can be greatly offset by the use of multiple sensors, in our case four. They are spaced as in Fig. 1, so as to have a signal from a local source on the interior sensors, but not on the exterior sensors. For an interfering signal far enough away to produce a linear gradient, the observable signal on a single sensor at position **r** with respect to the center of the field coils is, in phasor notation,

$$B_x(\mathbf{r}) + iB_y(\mathbf{r}) = B_x(0) + iB_y(0) \\ + \mathbf{r}\cdot[\nabla B_x(\mathbf{r}) + i\nabla B_y(\mathbf{r})]_{\mathbf{r}=0}. \qquad (5)$$

Since the sensors are in a line, $\mathbf{r} = [x, 0, 0]$, the above simplifies to

$$B_x(x) + iB_y(x) = B_x(0) + iB_y(0) + x\left[\frac{\partial B_x}{\partial x} + i\frac{\partial B_y}{\partial x}\right]_{x=0}. \tag{6}$$

So under interference, the average signal for the exterior sensors, at $x = \pm d$, is $[B_x(0) + iB_y(0)]$, and the average signal for the interior sensors, at $x = \pm\delta$, is also $[B_x(0) + iB_y(0)]$. By subtracting the exterior sensor average $\Sigma_{\mathrm{ex}}$ from the interior sensor average $\Sigma_{\mathrm{in}}$, the linear interference is subtracted out and the signal from the local source is retained. Another, more formal and more scalable, way to represent this same idea is

$$\Sigma \equiv \begin{bmatrix} \Sigma_{\mathrm{in}} \\ \Sigma_{\mathrm{ex}} \end{bmatrix} = \lambda_S \mathbf{v}_S + \lambda_I \mathbf{v}_I, \tag{7}$$

where $\lambda_S$ and $\lambda_I$ are the signal and interference projection coefficients, respectively, and

$$\mathbf{v}_I = \begin{bmatrix} 1/\sqrt{2} \\ 1/\sqrt{2} \end{bmatrix}; \qquad \mathbf{v}_S = \begin{bmatrix} 1 \\ 0 \end{bmatrix}. \tag{8}$$

Note that while the unit vectors $\mathbf{v}_S$ and $\mathbf{v}_I$ are linearly independent, they are not orthogonal. The projection coefficients can be approximated for any given data,

$$\Sigma = \mathbf{A}\lambda, \quad \text{where} \tag{9}$$

$$\mathbf{A} \equiv [\mathbf{v}_I \quad \mathbf{v}_S], \quad \text{and} \tag{10}$$

$$\lambda \equiv \begin{bmatrix} \lambda_S \\ \lambda_I \end{bmatrix}, \tag{11}$$

by choosing $\lambda$ to minimize the norm of $\Sigma - \mathbf{A}\lambda$, or in MATLAB [59], $\lambda = \mathbf{A}\backslash\Sigma$.

With heterodyne detection a complex signal is created in the time domain; after Fourier transform, the resulting signal in the frequency domain is also complex. The phase of the test signal is controlled, and the real part of the $\mathrm{Re}\{\lambda_S\} = \lambda'_S$ is therefore the appropriate figure of merit, and represents the local signal size. The phase of the interference is random with respect to data acquisition, therefore $|\lambda_I|$ is the more appropriate metric, and represents $\sqrt{2}$ times the interfering signal. These projection coefficients for both the resonant and interference peaks in the spectra of Fig. 10(d) are given in units of fT. The distribution of projection coefficients corresponding to a single point in the spectrum gives a more detailed perspective of the relative contributions to the net signal from a local source compared to an interfering source. In Fig. 10(e), the distribution of resonant projection coefficients $\lambda'_S$ and $\lambda'_I$ are shown, with $\lambda'_S$ clustered around the true value of the local signal and $\lambda'_I$ randomly distributed about zero. The distribution of $\lambda'_I$ is much larger when the resonance frequency is closer to the interference frequency, as can be seen by comparison with the inset of Fig. 10(e).

Using this algorithm on the four sensors, the sensitivity is retained when far off resonance from interference, as can be seen by the standard deviation in Figs. 10(a) and 10(b) compared to Figs. 10(c) and 10(d), illustrated with the red dotted lines. More importantly, the noise is reduced by a factor of 20 when the magnetometer is tuned close to interference, and the signal which is unobservable with only a single sensor can now be clearly observed. Here again, the use of the 2D spectrum, 10(d), shows the emergence of the local signal on the shoulder of the remnant interference peak.

The above data correspond to the ∥ direction, for which the interference signal is quite large. In the ⊥ direction the interference signal is 14× smaller. Not only is it smaller, but it is not as linear. Therefore, the radio-station signal in this case is reduced by only a factor of 4 at its maximum as opposed to the 26 seen in the parallel case. Nevertheless, after application of the interference algorithm, the sensitivity improves and is consistent with values observed when there is no interfering signal.

To examine the linearity of the signal, the peak of the interference in the 2D spectrum is plotted as a function of normalized position, $u = x/d$ in Fig. 11. The size of the signal is normalized and phased with respect to inner sensor 1 and the data shown are representative of what is consistently observed for the radio-station interference. The complex radio signals for the two configurations are fit to parabolas. The dominant term is the constant in either case. In the ⊥ orientation, however, there is a significant

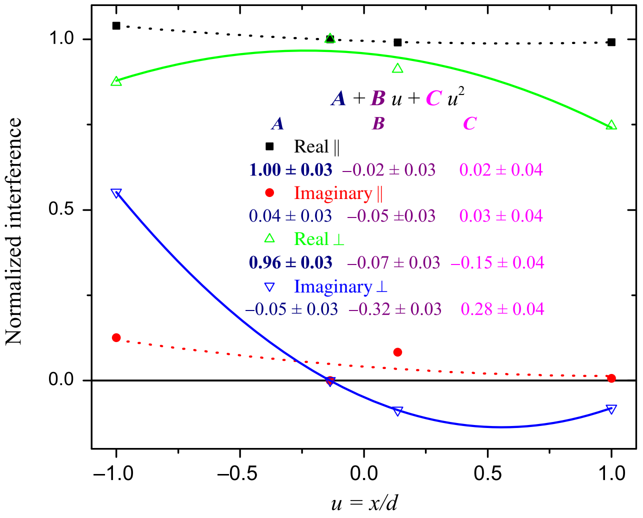

FIG. 11. The interference signal is plotted for the sensor array as a function of position, normalized to $d$, revealing the quadratic component is more significant in the ⊥ orientation than in the ∥. In the graph, the signals have been normalized to the complex signal of inner sensor 1, Fig. 1, to better show the functional dependence. The interference is, however, more than an order of magnitude higher for the ∥ orientation.

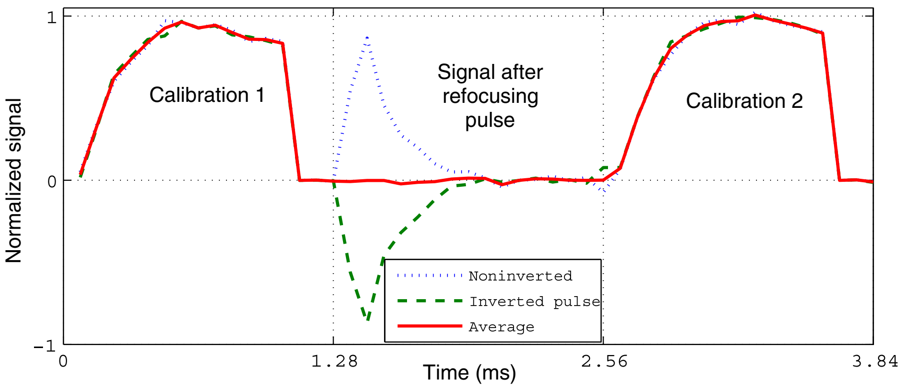

FIG. 12. The strong rf pulse used to excite the sodium-nitrite sample induces a phase-dependent ringing in the magnetometer which is reduced by averaging, solid red line, over the phase-cycled data, dashed and dotted data. Calibration data, taken just before and after the NQR echo train, are used to correct for drift in the magnetic field. Each curve corresponds to an average over $N$ echoes, Table II. The NQR signal is more than 2 orders of magnitude smaller than the calibration signal and would not be easily seen on the scale displayed.

quadratic term, particularly in the imaginary component, while in the ∥ orientation the real and imaginary quadratic coefficients are consistent with zero. The second-order correction to the Taylor-series expansion would be a quadratic term. The quadratic term becomes significant when the source of the interfering signal approaches that of the displacement of the outer sensors, $d = 12.5$ cm. Reradiation of the radio station by nearby metallic objects is therefore suspect. It seems reasonable that the contribution to the net magnetic field from reradiation would be more easily observable when the sensors are oriented so as to be insensitive to the incoming magnetic field. While we move large metal objects away from the sensors, the square Helmholtz coils cannot be easily removed. Common mode and differential ac currents are choked out at the input to the field coils, but this does not prevent local generation of current in the wire and, therefore, magnetic field. A quadratic dependence on position can occur only if the electric field varies over the rectangular structure. Using a simple 2-foot-long telescopic antenna, we find the electric field varies in any given direction by as much as a factor of 3 across the structure. Future work will focus on minimizing the reradiation footprint of the multiturn field coils, including reducing the effective net diameter of the wires down from 1/2” and considering other shapes.

### C. Nuclear quadrupole resonance

The same array of sensors, in the ⊥ orientation, is used to detect NQR signals from 63 g of $\mathrm{NaNO_2}$ potted in wax to reduce piezoelectric effects. The two inner sensors are $r \simeq 2$–3 cm, from the sample bottom and the outer 13 cm away. Given the steep dropoff of signal, $\sim 1/r^3$, the signal in the outer two sensors is negligible. Coherent ringing results from the application of rf pulses, Fig. 2 and Table II, but is mitigated by phase cycling, Fig. 12; a spin-lock spin-echo SLSE sequence [52] is used in which the phase of the refocusing pulse is flipped with every other scan. Stronger light pulses would also mitigate rf-induced ringing. The rf frequency is determined by the temperature $T_s$ of the sample, $f(T_s) = [1036.75 - 0.960\{T_s(^\circ\mathrm{C}) - 24\}]$ kHz; a boron-nitride sleeve, fitted around the sample, and inside the excitation coil, is used to make the temperature homogenous.

The strength $B_1$ of the excite pulse is varied and the result shown in Fig. 13. For a homogeneously excited powdered sample, the NQR signal [60] is $S(\vartheta) \propto J_{3/2}(\vartheta)/\sqrt{\vartheta}$, where $\vartheta = \gamma_N B_1 t_e$ and $\gamma_N$ is the nuclear gyromagnetic ratio of $^{14}$N. The data fit well to this function, Fig. 13, especially considering that the excitation is not uniform across the sample; the sample vertically fills the 2.5-cm-high pucklike excitation coil, Fig. 1. For optimal excitation, estimated signals are $26 + i8$ fT for inner sensor 2 and $13 - i2$ fT for inner sensor 1; estimates take into account the quantity of material, the size of the sample, the asymmetric positions of the sensors, and the decay across the echo train. The maximum signals measured are $21 + i9$ fT $\pm 1.7$, (23 fT/$\sqrt{\mathrm{Hz}}$) for the inner sensor 2

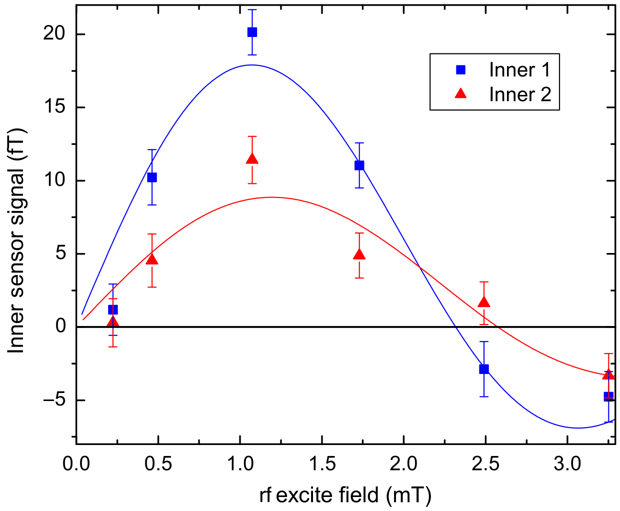

FIG. 13. The NQR signal detected by the two inner sensors is measured as a function of the excitation field strength. The difference in the results comes from asymmetric placement of the sensors with respect to the sodium nitrite sample; for RFIM the placement is made symmetric as shown in Fig. 1.

and $12 - i4$ fT ± 1.6 (22 $\mathrm{fT}/\sqrt{\mathrm{Hz}}$) for the inner sensor 1, close to what is estimated.

For the measurement made in Fig. 13, 120 echoes are used with a spacing of $t_0 = 1.2$ ms, Fig. 2. To get a high signal-to-noise ratio, ∼10, the measurement is repeated 1200 times. Using the 50-pass magnetometer, with over an order of magnitude better sensitivity, this repetition number would reduce down to 7, or with $2T_1$ recovery time between experiments [61], a 7-sec measurement in total.

## IV. CONCLUSIONS

An array of 2-pass rf atomic magnetometers, each with an effective volume of only 0.36 $\mathrm{cm}^3$, is used to detect a 100-fT signal with 0.5-Hz resolution amid a 200× larger AM radio field centered only 2.5 Hz away. Data acquisition is a second long and yields a signal-to-noise ratio of 2. The four-sensor array is designed to suppress rf magnetic interference that linearly varies in space. The chief limitation to the suppression comes from quadratic variation of the field across the sensors, most likely due to the reradiation of the interference from the Earth's field compensation coils surrounding the sensors. Future work will entail a smaller footprint for these field coils to minimize the reradiation and maximize the interference suppression.

Presently, the interference suppression, 26 dB, is similar to the suppression demonstrated with a coil-based gradiometer [29]. The magnetometer array is limited by reradiation from local coils; the coil-based gradiometer by capacitive coupling to the local environment, a limitation the magnetometer does not share. Moreover, magnetometers can be used as second-order or even higher-order gradiometers using an array of sensors without mutual inductive coupling. Therefore, if local reradiation can be eliminated, we expect that interference rejection solely due to distant sources should double in decibels from that of an ideal two-component gradiometer.

When placed in an orientation insensitive to and far off resonance in frequency from the radio interference, the array gives a sensitivity of 14 $\mathrm{fT}/\sqrt{\mathrm{Hz}}$, in agreement with photon-shot-noise limits. With a 50-pass magnetometer, of similar effective volume as the 2-pass magnetometer, the maximum optical rotation and the sensitivity are improved by an order of magnitude, showing the potential of such compact sensors. We find that the 50-pass magnetometer is fundamentally limited by spin-projection and light-shift noise, not photon-shot noise. The demonstrated sensitivity of the 50-pass cell, 1.7 $\mathrm{fT}/\sqrt{\mathrm{Hz}}$, is still not, however, entirely limited by fundamental noise sources. The noise peak is significantly enhanced due to ringing caused by the shut down of the pump laser. Under ideal conditions the area under the noise peak for polarized $^{87}\mathrm{Rb}$ atoms should be *smaller* than the area under noise bump due to unpolarized atoms [62]. The light-shift noise can be eliminated by stroboscopic modulation of the probe laser [62]. Furthermore, the 50-pass beam pattern presently fills only about 25% of the cell volume. With further optimization of these parameters, as well as using K atoms with a longer spin relaxation time, we expect to achieve sensitivity on the order of 0.3 $\mathrm{fT}/\sqrt{\mathrm{Hz}}$, similar to what is achieved using K atoms in a 400× large volume cell [17]. The scaling down of the atomic magnetometer in volume, without loss of sensitivity, has potentially revolutionary effects in many research areas, as it allows for better spatial resolution of magnetic fields.

In addition, unshielded detection of 63 g of sodium nitrite, 2 cm away, is demonstrated with the 2-pass array. With a similar array of 50-pass magnetometers, scaling for the differences in measured sensitivity, it should be possible to detect the same sample with a signal-to-noise ratio of 4 with a single 0.3-sec-long echo train.

## ACKNOWLEDGMENTS

We would like to acknowledge helpful discussions with Brian L. Mark of the Electrical and Computer Engineering Department at George Mason University. This work was supported by DARPA Contract No. HR0011-13-C-0058.

[1] International Telecommunication Union, http://www.itu.int (2016).

[2] I. M. Savukov, S. J. Seltzer, and M. V. Romalis, Detection of NMR signals with a radio-frequency atomic magnetometer, J. Magn. Reson. **185**, 214 (2007).

[3] H. Xia, A. Ben-Amar Baranga, D. Hoffman, and M. V. Romalis, Magnetoencephalography with an atomic magnetometer, Appl. Phys. Lett. **89**, 211104 (2006).

[4] J. Belfi, G. Bevilacqua, V. Biancalana, S. Cartaleva, Y. Dancheva, and L. Moi, Cesium coherent population trapping magnetometer for cardiosignal detection in an unshielded environment, J. Opt. Soc. Am. B **24**, 2357 (2007).

[5] G. Bison, N. Castagna, A. Hofer, P. Knowles, J.-L. Schenker, M. Kasprzak, H. Saudan, and A. Weis, A room temperature 19-channel magnetic field mapping device for cardiac signals, Appl. Phys. Lett. **95**, 173701 (2009).

[6] Cort Johnson, Peter D. D. Schwindt, and Michael Weisend, Magnetoencephalography with a two-color pump-probe, fiber-coupled atomic magnetometer, Appl. Phys. Lett. **97**, 243703 (2010).

[7] K. Kamada, Y. Ito, and T. Kobayashi, Human MCG measurements with a high-sensitivity potassium atomic magnetometer, Physiol. Meas. **33**, 1063 (2012).

[8] Kiwoong Kim, Samo Begus, Hui Xia, Seung-Kyun Lee, Vojko Jazbinsek, Zvonko Trontelj, and Michael V. Romalis, Multi-channel atomic magnetometer for magnetoencephalography: A configuration study, NeuroImage **89**, 143 (2014).

[9] Orang Alem, Tilmann H Sander, Rahul Mhaskar, John LeBlanc, Hari Eswaran, Uwe Steinhoff, Yoshio Okada, John Kitching, Lutz Trahms, and Svenja Knappe, Fetal

magnetocardiography measurements with an array of microfabricated optically pumped magnetometers, Phys. Med. Biol. **60**, 4797 (2015).

[10] Anthony P. Colombo, Tony R. Carter, Amir Borna, Yuan-Yu Jau, Cort N. Johnson, Amber L. Dagel, and Peter D. D. Schwindt, Four-channel optically pumped atomic magnetometer for magnetoencephalography, Opt. Express **24**, 15403 (2016).

[11] H. B. Dang, A. C. Maloof, and M. V. Romalis, Ultrahigh sensitivity magnetic field and magnetization measurements with an atomic magnetometer, Appl. Phys. Lett. **97**, 151110 (2010).

[12] I. M. Savukov and M. V. Romalis, NMR detection with an atomic magnetometer, Phys. Rev. Lett. **94**, 123001 (2005).

[13] Shoujun Xu, Valeriy V. Yashchuk, Marcus H. Donaldson, Simon M. Rochester, Dmitry Budker, and Alexander Pines, Magnetic resonance imaging with an optical atomic magnetometer, Proc. Natl. Acad. Sci. U.S.A. **103**, 12668 (2006).

[14] Giuseppe Bevilacqua, Valerio Biancalana, Andrei Ben-Amar Baranga, Yordanka Dancheva, and Claudio Rossi, Microtesla NMR J-coupling spectroscopy with an unshielded atomic magnetometer, J. Magn. Reson. **263**, 65 (2016).

[15] I. M. Savukov, V. S. Zotev, P. L. Volegov, M. A. Espy, A. N. Matlashov, J. J. Gomez, and R. H. Kraus Jr., MRI with an atomic magnetometer suitable for practical imaging applications, J. Magn. Reson. **199**, 188 (2009).

[16] I. Savukov and T. Karaulanov, Anatomical MRI with an atomic magnetometer, J. Magn. Reson. **231**, 39 (2013).

[17] S.-K. Lee, K. L. Sauer, S. J. Seltzer, O. Alem, and M. V. Romalis, Subfemtotesla radio-frequency atomic magnetometer for detection of nuclear quadrupole resonance, Appl. Phys. Lett. **89**, 214106 (2006).

[18] M. Schmelz, V. Zakosarenko, A. Chwala, T. Schönau, R. Stolz, S. Anders, S. Linzen, and H.-G. Meyer, Thin-film-based ultralow noise SQUID magnetometer, IEEE Trans. Appl. Supercond. **26**, 1 (2016).

[19] I. K. Kominis, T. W. Kornack, J. C. Allred, and M. V. Romalis, A subfemtotesla multichannel atomic magnetometer, Nature (London) **422**, 596 (2003).

[20] I. M. Savukov, S. J. Seltzer, M. V. Romalis, and K. L. Sauer, Tunable Atomic Magnetometer for Detection of Radio-Frequency Magnetic Fields, Phys. Rev. Lett. **95**, 063004 (2005).

[21] I. Savukov, T. Karaulanov, and M. G. Boshier, Ultra-sensitive high-density Rb-87 radio-frequency magnetometer, Appl. Phys. Lett. **104**, 023504 (2014).

[22] S. Li, P. Vachaspati, D. Sheng, N. Dural, and M. V. Romalis, Optical rotation in excess of 100 rad generated by Rb vapor in a multipass cell, Phys. Rev. A **84**, 061403 (2011).

[23] D. Sheng, S. Li, N. Dural, and M. V. Romalis, Subfemtotesla Scalar Atomic Magnetometry Using Multipass Cells, Phys. Rev. Lett. **110**, 160802 (2013).

[24] David A. Keder, David W. Prescott, Adam W. Conovaloff, and Karen L. Sauer, An unshielded radio-frequency atomic magnetometer with sub-femtotesla sensitivity, AIP Adv. **4**, 127159 (2014).

[25] Giuseppe Bevilacqua, Valerio Biancalana, Piero Chessa, and Yordanka Dancheva, Multichannel optical atomic magnetometer operating in unshielded environment, Appl. Phys. B **122**, 103 (2016).

[26] P. B. Roemer, W. A. Edelstein, C. E. Hayes, S. P. Souza, and O. M. Mueller, The NMR phased array, Magn. Reson. Med. **16**, 192 (1990).

[27] Lorena Cardona, Yuji Miyato, Hideo Itozaki, Jovani Jiménez, Nelson Vanegas, and Hideo Sato-Akaba, Remote detection of ammonium nitrate by nuclear quadrupole resonance using a portable system, Appl. Magn. Reson. **46**, 295 (2015).

[28] T. Munsat, W. M. Hooke, S. P. Bozeman, and S. Washburn, Two new planar coil designs for a high pressure radio frequency plasma source, Appl. Phys. Lett. **66**, 2180 (1995).

[29] B. H. Suits, The noise immunity of gradiometer coils for $^{14}$N NQR land mine detection: Practical limitations, Appl. Magn. Reson. **25**, 371 (2004).

[30] Bryan H. Suits, Nuclear quadrupole resonance spectroscopy, in *Handbook of Applied Solid State Spectroscopy*, edited by R. D. Vij (Springer, Boston, 2006), pp. 65–96.

[31] Christian Fernandez and Marek Pruski, *Probing quadrupolar nuclei by solid-state NMR spectroscopy: Recent Advances*, in Solid State NMR, edited by C. Jerry and C. Chan (Springer, Berlin, Heidelberg, 2012), pp. 119–188.

[32] A. N. Garroway, M. L. Buess, J. B. Miller, B. H. Suits, A. D. Hibbs, G. A. Barrall, R. Matthews, and L. J. Burnett, Remote sensing by nuclear quadrupole resonance, IEEE Trans. Geosci. Remote Sens. **39**, 1108 (2001).

[33] Joel B. Miller and Geoffrey A. Barrall, Explosives detection with nuclear quadrupole resonance: An emerging technology will help to uncover land mines and terrorist bombs, Am. Sci. **93**, 50 (2005).

[34] Joel B. Miller, in *Counterterrorist Detection Techniques of Explosives*, edited by Jehuda Yinon (Elsevier Science B.V., Amsterdam, 2007), Chap. 7, pp. 157–198.

[35] Joel B. Miller, Nuclear quadrupole resonance detection of explosives: An overview, Proc. SPIE Int. Soc. Opt. Eng. **8017**, 801715 (2011).

[36] Junichiro Shinohara, Hideo Sato-Akaba, and Hideo Itozaki, Nuclear quadrupole resonance of methamphetamine hydrochloride, Solid State Nucl. Magn. Reson. **43–44**, 27 (2012).

[37] J. Barras, K. Althoefer, M. D. Rowe, I. J. Poplett, and J. A. S. Smith, The emerging field of medicines authentication by nuclear quadrupole resonance spectroscopy, Appl. Magn. Reson. **43**, 511 (2012).

[38] Janez Seliger, Veselko Agar, Toma Apih, Alan Gregorovi, Magdalena Latosiska, Grzegorz Andrzej Olejniczak, and Jolanta Natalia Latosiska, Polymorphism and disorder in natural active ingredients. Low and high-temperature phases of anhydrous caffeine: Spectroscopic ((1)H-(14)N NMR-NQR/(14)N NQR) and solid-state computational modelling (DFT/QTAIM/RDS) study, European Journal of pharmaceutical sciences **85**, 18 (2016).

[39] C. Chen, F. Zhang, J. Barras, K. Althoefer, S. Bhunia, and S. Mandal, Authentication of medicines using nuclear quadrupole resonance spectroscopy, IEEE/ACM Trans. Comput. Biol. Bioinf. **13**, 417 (2016).

[40] Zheng Li, Yosuke Ooe, Xian-Cheng Wang, Qing-Qing Liu, Chang-Qing Jin, Masanori Ichioka, and Guo qing Zheng,

$^{75}$As NQR and NMR studies of superconductivity and electron correlations in iron arsenide LiFeAs, J. Phys. Soc. Jpn. **79**, 083702 (2010).

[41] J. Yang, Z. T. Tang, G. H. Cao, and Guo-qing Zheng, Ferromagnetic Spin Fluctuation and Unconventional Superconductivity in $Rb_2Cr_3As_3$ Revealed by $^{75}$As NMR and NQR, Phys. Rev. Lett. **115**, 147002 (2015).

[42] Q.-P. Ding, P. Wiecki, V. K. Anand, N. S. Sangeetha, Y. Lee, D. C. Johnston, and Y. Furukawa, Volovik effect and Fermi-liquid behavior in the $s$-wave superconductor $CaPd_2As_2$: $^{75}$As NMR-NQR measurements, Phys. Rev. B **93**, 140502 (2016).

[43] T. Apih, V. Agar, and J Seliger, NMR and NQR study of above-room-temperature molecular ferroelectrics diisopropylammonium chloride and diisopropylammonium perchlorate, J. Phys. Chem. C **120**, 6180 (2016).

[44] D. K. Walter, W. M. Griffith, and W. Happer, Energy Transport in High-Density Spin-Exchange Optical Pumping Cells, Phys. Rev. Lett. **86**, 3264 (2001).

[45] Tecmag Inc., http://www.tecmag.com (2015).

[46] M. E. Rudd and J. R. Craig, Optimum spacing of square and circular coil pairs, Rev. Sci. Instrum. **39**, 1372 (1968).

[47] P-8 Pro Series II from Furman Sound, http://www.furmansound.com/ (2014).

[48] Marcel J. E. Golay, Field homogenizing coils for nuclear spin resonance instrumentation, Rev. Sci. Instrum. **29**, 313 (1958).

[49] B. H. Suits and D. E. Wilken, Improving magnetic field gradient coils for NMR imaging, J. Phys. E **22**, 565 (1989).

[50] D. I. Hoult and R. E. Richards, The signal-to-noise ratio of the nuclear magnetic resonance experiment, J. Magn. Reson. (1969) **24**, 71 (1976).

[51] P. R. Robinson, Improvements to the system of four equiradial coils for producing a uniform magnetic field, J. Phys. E **16**, 39 (1983).

[52] R. A. Marino and S. M. Klainer, Multiple spin echoes in pure quadrupole resonance, J. Chem. Phys. **67**, 3388 (1977).

[53] Orang Alem, Karen L. Sauer, and Mike V. Romalis, Spin damping in an rf atomic magnetometer, Phys. Rev. A **87**, 013413 (2013).

[54] V. Shah, G. Vasilakis, and M. V. Romalis, High Bandwidth Atomic Magnetometery with Continuous Quantum Nondemolition Measurements, Phys. Rev. Lett. **104**, 013601 (2010).

[55] I. S. Gradshteyn and I. M. Ryzhik, *Table of Integrals, Series, and Products*, 7th ed. (Elsevier/Academic Press, Amsterdam, 2007), pp. xlviii and 1171 (translated from Russian).

[56] D. Sheng, S. Li, N. Dural, and M. V. Romalis, Subfemtotesla Scalar Atomic Magnetometry Using Multipass Cells, Phys. Rev. Lett. **110**, 160802 (2013).

[57] S. Appelt, A. B. Baranga, C. J. Erickson, M. V. Romalis, A. R. Young, and W. Happer, Theory of spin-exchange optical pumping of $^3$He and $^{129}$Xe, Phys. Rev. A **58**, 1412 (1998).

[58] W. C. Chen, T. R. Gentile, T. G. Walker, and E. Babcock, Spin-exchange optical pumping of $^3$He with Rb-K mixtures and pure K, Phys. Rev. A **75**, 013416 (2007).

[59] MATLAB version 7.14.0.739 (R2012a), Natick, Massachusetts (2012).

[60] Shimon Vega, Theory of $T_1$ relaxation measurements in pure nuclear quadrupole resonance for spins $I = 1$, J. Chem. Phys. **61**, 1093 (1974).

[61] G. Petersen and P. J. Bray, $^{14}$N nuclear quadrupole resonance and relaxation measurements of sodium nitrite, J. Chem. Phys. **64**, 522 (1976).

[62] G. Vasilakis, V. Shah, and M. V. Romalis, Stroboscopic Backaction Evasion in a Dense Alkali-Metal Vapor, Phys. Rev. Lett. **106**, 143601 (2011).